Medium-Range Order Structure Controls Thermal Stability of Pores in Zeolitic Imidazolate Frameworks

Christensen, Rasmus; Bleile, Yossi; Sørensen, Søren Strandskov; Biscio, Christophe; Fajstrup, Lisbeth; Smedskjær, Morten Mattrup

Published in:
The Journal of Physical Chemistry Letters

DOI (link to publication from Publisher):
10.1021/acs.jpclett.3c00962

Publication date:
2023

Document Version
Accepted author manuscript, peer reviewed version

Medium-Range Order Structure Controls Thermal Stability of Pores in Zeolitic Imidazolate Frameworks

Rasmus Christensen[1], Yossi Bleile[2], Søren S. Sørensen[1], Christophe A. N. Biscio[2], Lisbeth Fajstrup[2], Morten M. Smedskjaer[1,*]

[1] *Department of Chemistry and Bioscience, Aalborg University, Aalborg, Denmark*

[2] *Department of Mathematical Sciences, Aalborg University, Aalborg, Denmark*

[*] Corresponding author. E-mail: mos@bio.aau.dk

Abstract

Metal-organic framework (MOF) glasses have multiple potential applications as they combine advantages of traditional glasses with those of MOFs. The melt-quenching process used to form MOF glasses typically leads to a significant decrease in porosity, but the structural origin of this thermally-induced pore collapse remains largely unknown. Here, we study the melting process of three zeolitic imidazolate frameworks (ZIFs), namely ZIF-4, ZIF-62, and ZIF-76, using *ab initio* molecular dynamics (MD) simulations. By analyzing the MD data using topological data analysis, we show that while the three ZIF systems exhibit similar short-range order structural changes upon heating, they exhibit significant differences in their medium-range order structure. Specifically, ZIF-76 retains more of its medium-range order structures in the liquid state compared to the other glass-forming ZIF systems, which allows it to remain more porous than ZIF-4 and ZIF-62. As such, our results may aid in understanding what structural features govern the ability to maintain porosity in the melt-quenched glassy state.

Table of Contents Graphic:

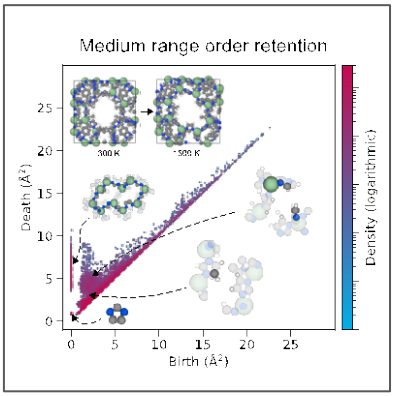

Metal-organic frameworks (MOFs) are composed of inorganic and organic building units, which interconnect to form crystalline porous coordination networks.[1,2] They have numerous potential uses within, e.g., gas storage and separation[3,4], catalysis[5], and drug delivery[6]. Typically, these crystalline compounds decompose irreversibly at elevated temperatures (200−600 °C)[7], but it has recently been shown that some MOFs can undergo melting before thermal decomposition[8,9]. In turn, this enables quenching of the molten MOF phase to a glassy state[10]. The most studied family of glass-forming MOFs so far is zeolitic imidazolate frameworks (ZIFs). These are based on metal ions like Co^{2+} or Zn^{2+} and imidazolate-based ligands forming tetrahedral short-range order (SRO) structural units (Figure 1A), which organize into larger medium-range order (MRO) network topologies comparable to those found in inorganic zeolites.

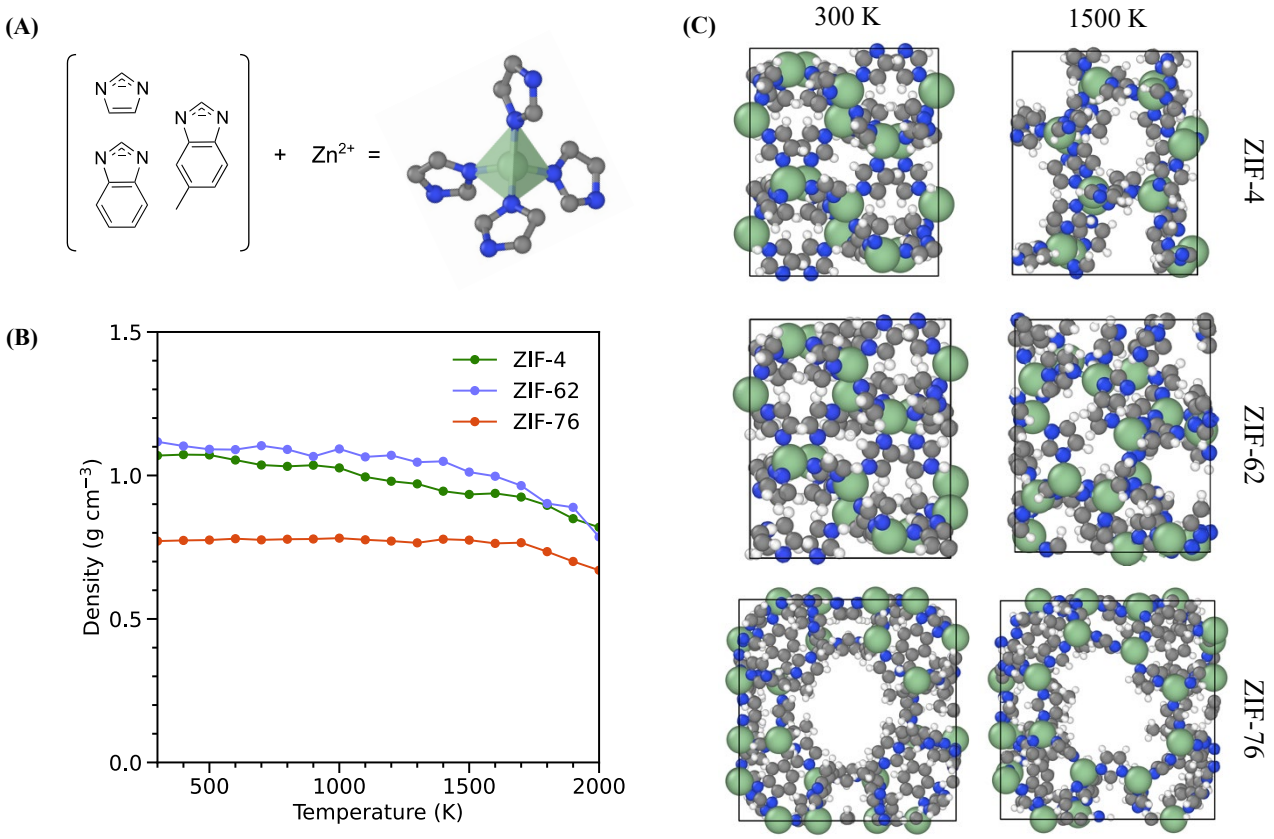

Figure 1. (A) Building blocks of the ZIF systems (Zn^{2+} and imidazolate-based ligands) forming a tetrahedral unit. (B) Density evolution upon heating from 300 to 2000 K for ZIF-4 (green), ZIF-62 (purple), and ZIF-76 (orange). (C) Atomic snapshots of the three ZIF systems at 300 K (first column) and 1500 K (second column). Zn, N, C, and H atoms are colored green, blue, grey, and white, respectively.

It has been demonstrated that crystallinity is not required for achieving many of the attractive properties of MOFs and certain compositions can feature accessible porosity in the glass state[10,11]. However, the retention of accessible porosity in MOF glasses is challenging because the pore cavities generally collapse into a dense, disordered phase upon melt-quenching. For example, this is the case for the well-studied ZIF-4 ($Zn(Im)_2$, where Im is imidazolate), which exhibits no significant N_2 uptake and reduced CO_2 uptake in its glassy state compared to the corresponding crystal phase[9,12]. Pore collapse is, however, not a given in MOF glasses. For example, the degree of pore collapse in ZIF-62 ($ZnIm_{1.75}bIm_{0.25}$, where bIm is benzimidazolate) depends on

the processing conditions[4], and partial retention of porosity after melt quenching has been observed in some other ZIF systems, including Co-ZIF-62[13], ZIF-76-ClbIm ($Zn(Im)_{1.62}(ClbIm)_{0.38}$, where ClbIm is chlorobenzimidazolate) and ZIF-76-mbIm ($Zn(Im)_{1.33}(mbIm)_{0.67}$, where mbIm is methylbenzimidazolate) glasses.[14] In the two ZIF-76 based glasses, MRO in the crystal state was partially preserved in the glass phase as observed from retention of features above 6 Å in the experimentally measured pair distribution functions.[14] In detail, it was found that a mixture of crystalline TIF-4 ($Zn(Im)_{1.8}(mbIm)_{0.2}$) and crystalline ZIF-76-ClbIm or ZIF-76-mbIm is needed for glass formation to occur in this system, as neither phase pure ZIF-76-ClIm (Zn(Im)(ClbIm)) nor ZIF-76-mbIm (Zn(Im)(mbIm)) can melt independently.[15]

To enable fabrication of MOF glasses with accessible porosity, an understanding of what controls the thermally induced pore collapse during melting is needed. In this work, we present a computational study of the melting mechanism of three ZIF frameworks: ZIF-4, ZIF-62, and ZIF-76-mbIm (referred to as ZIF-76 from hereon). We choose these systems due to their glass-forming ability and experimentally observed differences in the ability to retain porosity upon glass formation. To this end, computational methods such as *ab* initio molecular dynamics (AIMD) simulations enable mapping of the individual atom positions *in situ* and have previously been used to simulate the melting and glass formation process in various ZIFs[16–20]. Due to the complex nature of the liquid (disordered) structures, previous studies have focused mainly on descriptions of the local environment of atoms and porosity measurements through probe-occupiable volume calculations[16,17,19], possibly losing critical information in other structural regimes such as how the size and shape of pores evolve during melting. Furthermore, simulations were conducted in the *NVT* ensemble, restricting the structural space that was explored due to the fixed volume. Therefore, to observe changes in the porous volume of the ZIF systems during heating, we here use the *NPT* ensemble. The use of AIMD limits the size of our simulations to a few hundreds of atoms. As mentioned above, phase pure ZIF-76 does not melt, which presents a problem for AIMD as it is currently impossible to construct an accurate representation of the required TIF-4/ZIF-76 crystal mixture within the system size constraints due to the computational cost. We, therefore, choose to construct and simulate a ZIF-76 crystal with the LTA crystal topology and a ratio of imidazolate and methylbenzimidazolate equal to that of the TIF-4 and ZIF-76 mixture, which has been reported to melt and form a $Zn(Im)_{1.33}(mbIm)_{0.67}$ glass that exhibits a notable retention of porosity in the glassy state[14,15].

In this study, we also investigate the changes in MRO structures and porosity upon melting of ZIF systems in a different way, namely by analyzing the AIMD data using persistent homology from topological data analysis (TDA)[21,22] to describe the topological properties of the data. With potential applications in many fields, persistent homology can be used to analyze high-dimensional datasets that emphasize global characteristics like data shape and connectivity. A more comprehensive description of the computation of persistent homology is provided in Supporting Text 1 and Figure S1. Specifically, persistent homology has previously been used to successfully describe MRO structure of disordered materials such as silica and sodium silicate glasses[23–25]. One of the main summaries obtained from persistent homology is the persistence diagram, which is a two-dimensional visualization of both the fraction and scale of the structural features (e.g., rings and cavities) in the atomic configuration. The persistence diagram is calculated based on i) the atomic trajectories produced

from, e.g., MD simulations or reverse Monte Carlo analysis of diffraction data, and ii) the atomic radii. Persistent homology has the advantage over conventional ring size analyses that it gives a fingerprint of the both the short- and medium-range order structural features without being restricted to chemically bonded structures. To probe the evolution of the three ZIF structures upon melting, we performed AIMD simulation of a stepwise heating of the initial ZIF crystal structures from 300 to 2000 K in the *NPT* ensemble, corresponding to an effective heating rate of 40 K ps^{-1} (see details in the Methods section). The temperature and potential energy evolution as a function of time can be found in Supporting Figures S2 and S3, respectively. While such high temperatures and heating rates would not be experimentally possible for this system, the procedure is necessary due to the computational cost of the AIMD simulations[16,20]. As the simulations were conducted in the *NPT* ensemble, the densities of the crystals change during heating (Figure 1B). We find that the densities of both ZIF-4 and ZIF-62 decrease during heating, whereas that of ZIF-76 remains constant from 300 to 1700 K, whereafter it also decreases with temperature. The observed drops in density can be attributed to the thermal expansion of the crystals during heating, in agreement with previous observations of positive thermal expansion of the cag topology of ZIF-4 and ZIF-62[26]. The most pronounced decrease is observed at the highest temperatures (>1500 K), indicating that the systems begin to vaporize. The observed difference in density evolution for ZIF-76 compared to those of ZIF-4 and ZIF-62 indicates a higher thermal stability of the ZIF-76 crystal structure. Figure 1C shows a comparison of the three ZIF structures at 300 and 1500 K, respectively. Significant changes in the structures are observed upon heating to 1500 K. Namely, the porous structures found initially in the crystalline ZIF-4 and ZIF-62 samples reorganize into less dense phases but with different pore morphology. On the other hand, ZIF-76 retains its large cavity after heating to 1500 K, in agreement with the experimentally observed ability of TIF-4 and ZIF-76 mixtures to form porous glasses upon melt-quenching[14,15]. We note that the formation of a less dense liquid phase for ZIF-4 and ZIF-62 might seem counter intuitive, as glasses produced from ZIF liquids have generally been reported to lose porosity[9,12]. However, while the liquid near the glass transition may indeed feature low porosity, these less dense liquid phases are observed far above T_g and thus far away in conformational space to that of the frozen-in glass state (which is also the case in the experiments with $T_m > T_g$).

To further understand the structural evolution of the systems during melting, we next focus on the short-range order (SRO) structural changes. To this end, we first calculate the Zn-N (Figure 2A) and Zn-Zn (Figure 2B) partial radial distribution functions (RDF) to probe the interatomic correlations shown in Figure 2C. For all three ZIF compositions and both RDFs, we observe the same general trend, that is, a broadening and decreasing intensity of the peaks with increasing temperature. This trend has been also observed experimentally in the case of ZIF-4 based on total pair distribution functions[16]. To further quantify the peak broadening and estimate the melting temperature, we compute the Lindemann ratio (full width at half maximum of the first peak divided by the interatomic distance of the first peak) of the Zn-N RDF as a function of temperature (Figure 2D). As expected, the Lindemann ratio increases with increasing temperature and all three ZIFs follow essentially the same trend. We also observe the same behavior for the Lindemann ratio for the first peak in Zn-Zn RDF (Supporting Figure 4), but with lower values at all temperatures for all ZIFs. The

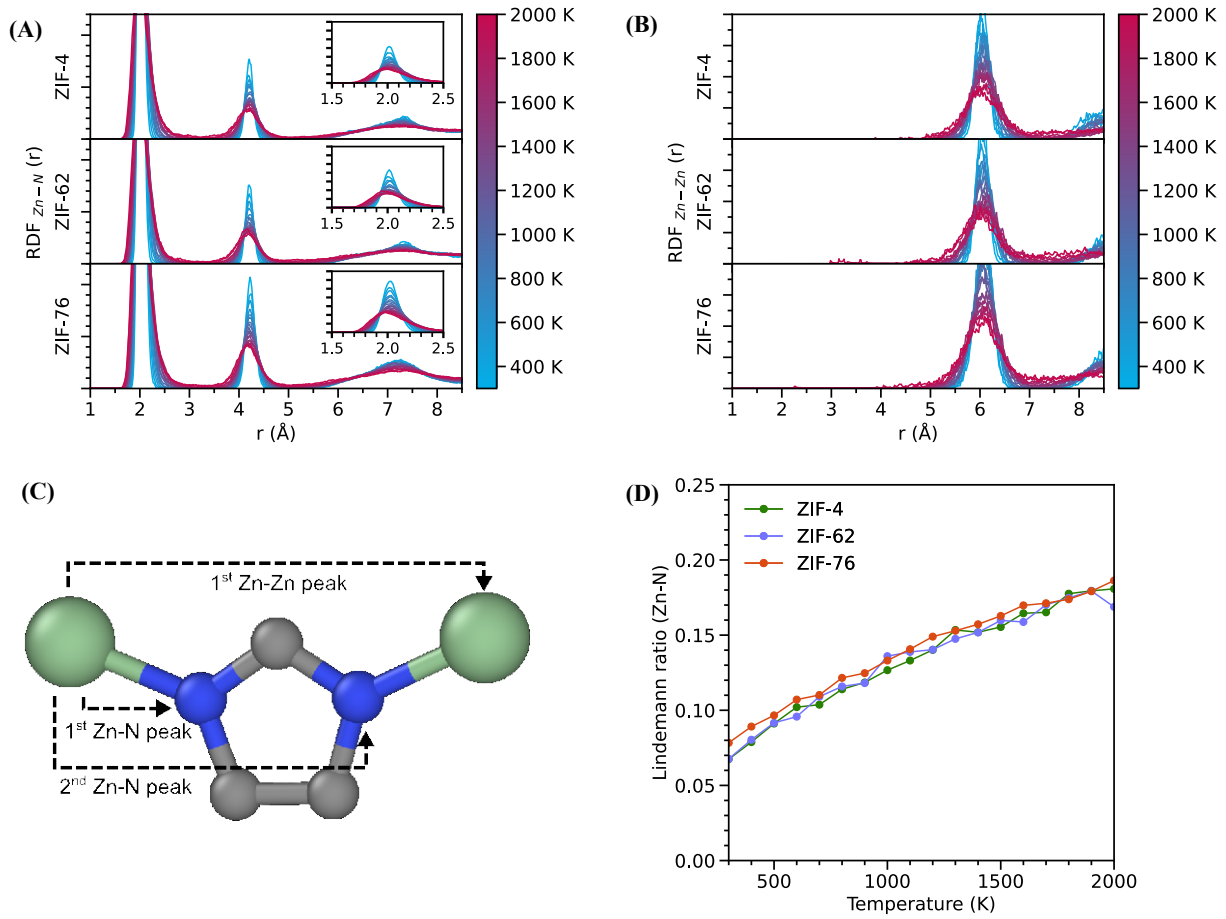

Figure 2. (A,B) Partial radial distribution functions of the atom pairs (A) Zn-N and (B) Zn-Zn for ZIF-4 (top), ZIF-62 (middle), and ZIF-76 (bottom). (C) Schematic view of the atomic origin of the radial distribution function peaks. (D) Temperature dependence of Lindemann ratio of the first peaks of the Zn-N pair distribution functions for ZIF-4 (green), ZIF-62 (purple), and ZIF-76 (orange).

common criterion used to determine melting from the Lindemann ratio is values between 0.10 and 0.15, which gives a melting temperature in the range of 600 and 1300 K when considering the Zn-N RDF for the three ZIFs. This range is fairly large but matches results from previous simulation studies,[16,17] indicating that in the present simulations, ZIF-76 in the LTA crystal topology with the given Im/mbIm ratio does indeed melt, contrary to the experimental observations for the phase pure ZIF-76 (Zn(Im)(mbIm))[15]. The experimental melting points of the ZIF systems have been estimated to be 603 K for ZIF-4[9,15], 703 K for ZIF-62[27] and 744 K for the phase mixture of TIF-4 and ZIF-76[14]. That is, while the experimental melting points of ZIF-systems are within the observed range, the trend in the experimental melting temperatures is not reproduced in the present simulations. However, we note that in experiments, ZIF-4 is known to recrystallize into the dense ZIF-zni phase after melting and this phase then melts at 866 K[9]. Such recrystallization is not observed in our simulations, most likely due to the limited timescale, but we note that the melting mechanism of ZIF-4 and ZIF-zni has been investigated previously using AIMD simulations[17].

To further investigate the SRO changes, we compute the Zn coordination number during heating (Figure 3A). Generally, we observe the same trend in Zn coordination changes for all three ZIF systems, namely the formation of undercoordinated Zn atoms in the systems as the temperature increases. Specifically, the

formation of three-fold coordinated Zn at around 1300 K and two-fold coordinated Zn at around 1900 K. The onset temperatures for these Zn coordination changes are higher than those previously reported for ZIF-4 by Gaillac et al.[16]. We ascribe this to the difference in the heating protocol, including a change of the ensemble (*NPT* vs. *NVT*). This is because the pressure increase, which can occur at high temperatures in the *NVT* ensemble, can potentially affect the thermodynamics of the systems including melting and glass transition temperatures[18,28].

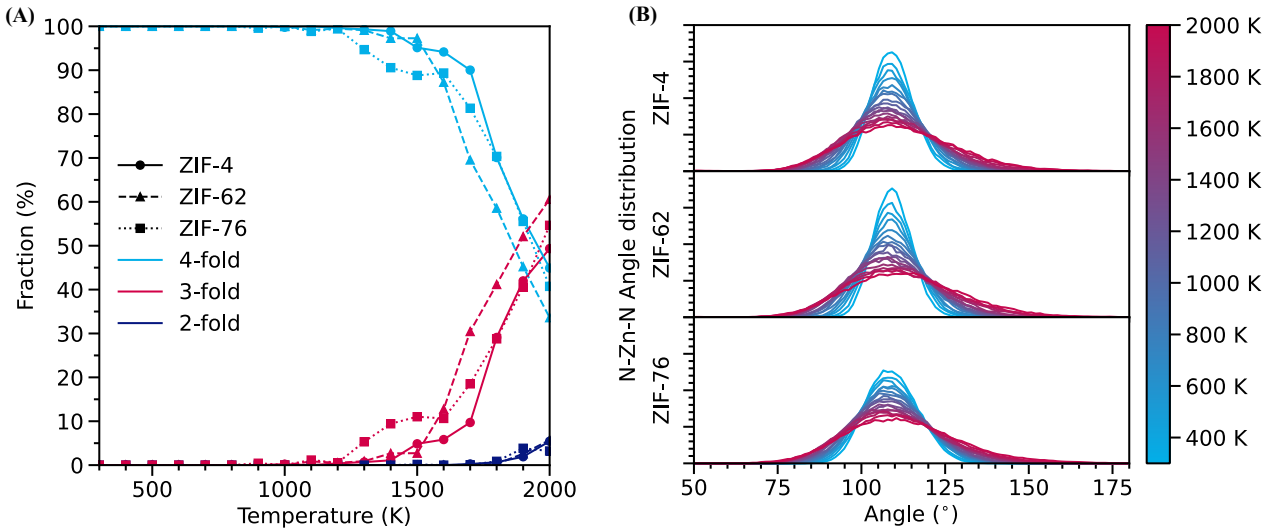

Figure 3. (A) Zn coordination number distributions, showing 4-fold (blue lines), 3-fold (red lines), and 2-fold (dark blue lines) coordination states as a function of temperature for ZIF-4 (circle points, full line), ZIF-62 (triangle points, dashed line), and ZIF-76 (square points, dotted line). (B) Evolution of N-Zn-N bond angle distributions from 300 K (blue line) to 2000 K (red line) for ZIF-4 (top), ZIF-62 (middle), and ZIF-76 (bottom).

While the RDFs provide a clear description of the SRO, they fail to capture more than two-body correlations. Therefore, we extend our analysis to calculate the N-Zn-N bond angle distribution evolution during heating (Figure 3B). A significant broadening of the bond angle distribution with increasing temperatures is observed, together with an increase in the average bond angle as three- and two-fold coordinated Zn atoms form. Interestingly, ZIF-76 has a wider initial bond angle distribution, indicating a less ordered initial local structure, probably owing to the steric effect of its larger organic linkers (methylbenzimidazolate), but reaches similar bond angle distributions as the other systems upon heating above 1000 K. The evolution of the full width half maximum of the bond angle distributions can be seen in Supporting Figure S5. Based on these analyses of RDFs, coordination numbers and bond angle distributions in the above, we conclude that the SRO structures of the different ZIF systems behave very similarly during heating, all becoming more disordered as the ZIF crystals begin to melt. However, in addition to SRO and the role of the metal-ligand bonds[29], it is well-known that structural features beyond the first coordination shell affect the behavior of glasses and glass-forming liquids[23,24,30]. Thus, to further understand how the ZIF structures change during heating, we investigate changes in their MRO and thus nanoscale porosity.

We evaluate the MRO changes using persistent homology (Figure 4A), but other commonly used methods such as ring size analysis, probe-occupiable volume analysis, and pore size distributions analysis were also computed (see Supporting Figures S6-S8). The results of these analyses correlate well with the results presented below, showing a decrease in the number of large rings (>6 atoms) and the formation of new ring sizes upon heating in all the ZIF systems. These traditional analyses also show an increase in the probe-occupiable volume and pore size distributions upon heating but mainly in the ZIF-4 and ZIF-62 systems. Then, we consider the persistence diagrams for both 1D (loops) and 2D (voids) as described in Supporting Text 1. The diagrams are computed for the three ZIFs at the different simulation temperatures. The collection of all persistence diagrams can be found in Supporting Figures S9-S11. As examples, we present the 1D persistence diagrams of the three different compositions at 300 K and 1500 K in Figure 4B. All the diagrams display a v-shape pattern with many loops that are born early (loops consisting of chemically bonded atoms as seen on Figure 4A) with varying death times (i.e., close to the vertical axis), and many points along the diagonal. Points near the diagonal have a short lifetime (d_i- b_i) and are often weighted less when comparing persistence diagrams (both qualitatively and quantitatively). In particular, a single point with a small lifetime will not drastically impact the (dis)similarity of two persistence diagrams, whereas many points with small lifetimes can provide a lot of information as a group, despite being less informative as individuals. As the temperature increases, the points spread more out, as the well-defined loop structures of the ZIF crystals change upon heating, resulting in more loops starting to occupy the region between early birth times and the diagonal. Such structures are non-intuitive in nature but result from correlations between atoms in different imidazolate units that are close in space, although not necessarily bonded to the same Zn atoms (see Figure 4A).

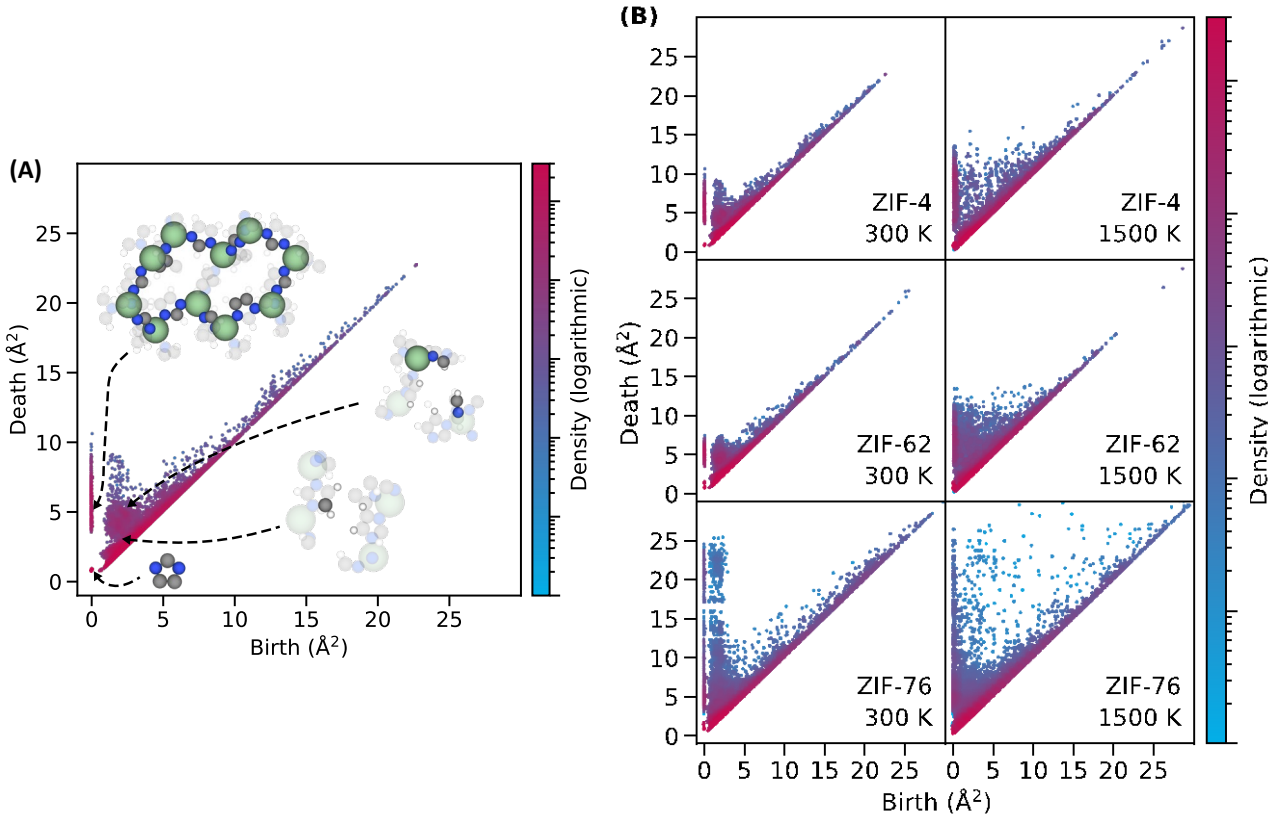

Figure 4. (A) 1D persistence diagram for ZIF-4 at 300 K with example of representative topological structures overlayed. The topological structures consist of the atoms with high opacity, while atoms with low opacity are neighboring atoms within 4 Å, included for reference. Zn, N, C, and H atoms are colored green, blue, grey, and white, respectively. (B) 1D persistence diagrams at 300 K (left) to 1500 K (right) for ZIF-4 (top), ZIF-62 (middle) and ZIF-76 (bottom). Points are colored logarithmically based on the point density in the diagrams.

In the 2D persistence diagrams shown in Supporting Figures S12-14, we again observe that the diagrams have many points along the diagonal, with specific areas in the diagram also containing many points. The locations of these areas vary depending on the ZIF system and correspond to the specific void structures of the given ZIF system. We observe similar behavior between ZIF-4 and ZIF-62 owing to their similar initial crystal structure. The scale of voids identified for ZIF-76 is much larger compared to that of ZIF-4 and ZIF-62, with points being born and dying later for ZIF-76, confirming that the large void structures in ZIF-76 can be identified. Like the 1D diagrams, we observe a widening effect with increasing temperature, especially when heating above 1600 K.

Although persistent homology is an effective tool for identifying both simple and non-obvious atomic structures, the comparison of persistence diagrams is difficult and mostly qualitative. To make quantitative comparisons, we also compute the accumulative persistence function (APF)[31] for the loops and voids of the studied ZIF structures (Figure 5). The APF is an accumulative sum of the lifetimes of points in the persistence diagram as a function of their mean age, $m = (b_i + d_i)/2$. The APF thus compiles the data from the persistence diagrams (e.g., Figure 4A) into a single non-continuous function, allowing for quantitative comparisons of the persistence diagrams as the ZIFs are heated (see Supporting Text 1 for further details about the APF). The 1D

APFs of the loops of all structures and temperatures are presented in Figures 5A-C. Here, we observe a shift in the distribution towards higher mean age with increasing temperature for ZIF-4 and ZIF-62, caused by the previously mentioned shift toward more loops occupying the region between early birth times and the diagonal. In comparison, the APF for ZIF-76 features only minor changes, mainly at high temperatures.

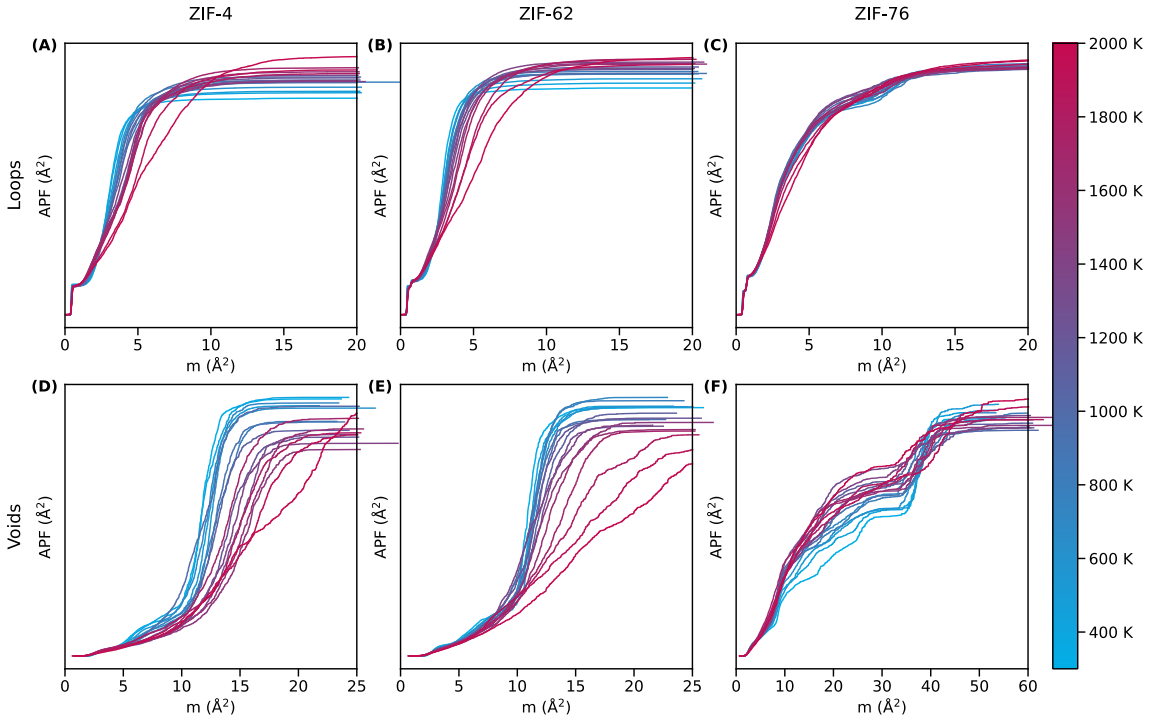

Figure 5. The evolution of the accumulative persistence functions (APFs) during heating from 300 K (blue line) to 2000 K (red line). The APFs are calculated for the loops of (A) ZIF-4, (B) ZIF-62, and (C) ZIF-76, and the voids of (D) ZIF-4, (E) ZIF-62, and (F) ZIF-76.

Similarly, when comparing the evolution of the APF of the 2D features (voids) presented in Figures 5D-F, we find that ZIF-4 and ZIF-62 show comparable evolution in their APF with a shift towards higher mean age with increasing temperature. Again, the APF for ZIF-76 is markedly different, remaining more stable with temperature. Taken as a whole, these findings indicate that the MRO loop and void structures in ZIF-76 crystals are more thermally stable, although ZIF-76 is the most porous crystal structure. The observed changes in the 2D APFs of ZIF-4 and ZIF-62 show the formation of a more porous structure upon heating as the mean age of void structures in these systems shifts towards higher values upon heating. This agrees with the observed decrease in density in these *NPT* simulations (Figure 1B). As the original MRO structures of the ZIF-4 and ZIF-62 crystals are essentially lost during heating, their crystal structures are not as thermally stable as those of ZIF-76. This could explain their loss in porosity after melt-quenching to the glass as seen in experiments. In contrast, we observe that the molten ZIF-76 phase to a much larger extent retains the topological characteristics of its crystal phase upon heating (Figure 5F).

Finally, we compare the observations from PH with the changes observed in the short-range order (broader radial and bond angle distributions and decreased Zn coordination). The observed SRO changes have an impact on the MRO structures in all the ZIF systems as Zn-N bonds are broken and atoms are rearranged. However, we observe that the topological features of the resulting MRO structures of the ZIF-76 remain more

stable compared to the ZIF-4 and ZIF-62 systems as seen by the APF. This indicates that as the MRO structures present in the ZIF-76 crystal are changed during heating, they reassemble into new structures with similar topological features, which help retain the large void in the center of the ZIF-76 unit cell during heating. For ZIF-4 and ZIF-62, the MRO structures reassemble into structures with different topological features, possibly explaining why these structures cannot retain their nanoscale porosity upon melt-quenching. This ability of the simulated ZIF-76 crystal to better retain MRO structures with similar topological features during heating matches well with the experimentally observed inability for phase pure Zn[(Im)(mbIm)] to form a melt[15]. However, our simulated ZIF-76 crystal does melt as shown by the decrease of the Zn-N coordination number with temperature (Figure 3A). This could be explained by the increased amount of imidazolate linker in the simulated ZIF-76 crystal (composition: $Zn(Im)_{1.33}(mbIm)_{0.67}$), resulting in less steric hinderance compared to the Zn(Im)(mbIm) crystal. The difference in meltability may therefore be attributed to the reduction in steric hindrance at the tetrahedral metal site, since such effect is known to lower the melting temperature, e.g., by facilitating linker dissociation in ZIF-62[32]. Relating this to the porous glass-forming phase mixture of TIF-4 and ZIF-76, this indicates that upon substitution of methylbenzimidazolate for imidazolate in the LTA crystal of phase pure ZIF-76, formation of melts with retained MRO structure can potentially occur.

In summary, our findings point to a link between the ability of ZIFs to retain porosity after melt-quenching and the ability to retain MRO structures of the crystal phase during heating, even when the extent of short-range disorder increases (coordination and bond angles). To verify this, further investigation of how MRO changes during melt-quenching is needed, especially from experiments. However, our findings appear to be in agreement with recent experimental work, showing how high-porosity in MOF glasses can be achieved by bridging and chelating binding modes to give more robust linkages[11]. As such, work provides the initial steps for understanding how to retain microporosity in MOF liquids and glasses through tailoring the MRO structures.

Computational methods

Ab initio molecular dynamics. The performed simulations were adapted based on the procedure outlined by Gaillac et al.[16,17]. Specifically, using the Quickstep package[33] in the CP2K software[34], *ab initio* molecular dynamics (AIMD) simulations were carried out, employing the Gaussian and Augmented plane wave approach. The exchange-correlation energy was assessed using the Perdew-Burke-Ernzhof (PBE) approximation[35]. Valence electrons were described by double-zeta valence polarized basis sets and norm-conserving Goedecker–Teter–Hutter pseudopotentials[36], all adapted using PBE (DZVP-GTH-PBE) for H, C and N or optimized for solids (DZVP-MOLOPT-SR-GTH) in the case of Zn. The dispersion interactions were handled at the DFT-D3 level[37]. The simulations were run in the *NPT* ensemble at zero pressure, with a Nose-Hoover thermostat and barostat used to regulate the temperature and pressure. The simulations employed a time step of 0.5 fs. We preserved the default number of four different grids and a plane-wave cutoff for the electronic density of 600 Ry. A relative cutoff of 40 Ry was used.

Melting simulations were conducted by first equilibrating the systems at 300 K for 6 ps, followed by incremental heating steps, raising the temperature by 100 K at each step until a maximum temperature of 2000 K was reached. Every heating step consisted of 2 ps equilibration and 0.5 ps recording of properties, resulting in an effective heating rate of 40 K/ps. Three repetitions of the simulations were conducted for each system, and all reported properties are averages of these.

Crystal structure preparation. The initial structures of the three ZIF crystals were generated in different ways depending on the available data. Common for all crystals was that a cell optimization was conducted to minimize the energy of the system before the AIMD simulation. The unit cell considered for ZIF-4 was taken from ref.[38], containing 272 atoms. For ZIF-62, the unit cell was taken from ref.[32] and adjusted to only include four benzimidazolate molecules on the reported favored positions in the structure[32], giving a total of 296 atoms. For ZIF-76, a unit cell of ZIF-76 (Zn(Imidazolate)(5-chlorobenzimidazolate)) was first obtained and then modified to exchange Cl atoms for methyl groups as well as exchange benzimidazolate groups for imidazolate groups to finally obtain a composition of Zn(imidazolate)$_{1.33}$(5-methylbenzimidazolate)$_{0.67}$ similar to that in ref. [14]. The final unit cell contains 552 atoms. The crystal unit cell parameters of the three systems after geometry optimization can be found in Supporting Table S1.

Topological data analysis. The python3 libraries Dionysus 2[39] and DioDe[40] were used to carry out persistent homology analyses. Persistence diagrams were computed from 3×3×3 replications of the simulation cells without periodic boundaries to account for atom correlations across the boundary. This approach is used instead of periodic alpha complexes due to software limitations. Replications of 5×5×5 and 7×7×7 were also investigated to evaluate the effect of the border conditions, but showed the same behavior in initial analyses, causing the choice of the 3×3×3 replication for computational efficiency. Weighted α-shapes were computed in DioDe using the atomic radii of r_{Zn} = 1.491 Å, r_H = 0.389 Å, r_C = 0.718 Å, and r_N = 0.635 Å as calculated from average bond lengths in three ZIF systems at 300 K.

Author Contributions

R.C. and M.M.S. conceived the study and planned the simulations. R.C. performed the AIMD simulations with input from S.S.S. R.C. performed the topological data analysis with input from Y.B., C.A.N.B. and L.F. M.M.S. supervised the project. All authors participated in discussing the data. R.C. wrote the manuscript with revisions from the other authors.

Notes

The authors declare no competing financial interest. The data supporting the results within this paper are available from the corresponding author upon request.

Supporting Information

Description on computation of persistence diagrams, Temperature and potential energy evolution during heating, Lindemann ratio of Zn-Zn RDF, Full width at half maximum of bond angle distributions, Ring size analysis, Probe-occupiable volume analysis, Pore size distributions, 1D and 2D persistence diagrams at 100K temperature intervals for the ZIF-systems, Crystal cell parameters.

Acknowledgements

This work was supported by the Independent Research Fund Denmark (1026-00037) and the Danish Data Science Academy, which in turn is funded by the Novo Nordisk Foundation (NNF21SA0069429) and VILLUM FONDEN (40516). We also thank the Danish e-Infrastructure Cooperation (DeiC) for access to computational resources at Sophia and LUMI-C (DeiC-AAU-N5-202200005).

References

(1) Kitagawa, S.; Matsuda, R. Chemistry of Coordination Space of Porous Coordination Polymers. *Coord. Chem. Rev.* **2007**, *251*, 2490–2509.

(2) Furukawa, H.; Cordova, K. E.; O'Keeffe, M.; Yaghi, O. M. The Chemistry and Applications of Metal-Organic Frameworks. *Science* **2013**, *341*, 1230444.

(3) Li, H.; Wang, K.; Sun, Y.; Lollar, C. T.; Li, J.; Zhou, H.-C. Recent Advances in Gas Storage and Separation Using Metal–Organic Frameworks. *Mater. Today* **2018**, *21*, 108–121.

(4) Smirnova, O.; Hwang, S.; Sajzew, R.; Reupert, A.; Nozari, V.; Savani, S.; Chmelik, C.; Wondraczek, L.; Kärger, J.; Knebel, A. Precise Control over Gas Transporting Channels in Zeolitic Imidazolate Framework Glasses. *ChemRxiv,* February 13, 2023, Version 1. https://doi.org/10.26434/chemrxiv-2023-b8nnx. (accessed 2023-31-07).

(5) Zhu, L.; Liu, X.-Q.; Jiang, H.-L.; Sun, L.-B. Metal–Organic Frameworks for Heterogeneous Basic Catalysis. *Chem. Rev.* **2017**, *117*, 8129–8176.

(6) Lawson, H. D.; Walton, S. P.; Chan, C. Metal–Organic Frameworks for Drug Delivery: A Design Perspective. *ACS Appl. Mater. Interfaces* **2021**, *13*, 7004–7020.

(7) Healy, C.; Patil, K. M.; Wilson, B. H.; Hermanspahn, L.; Harvey-Reid, N. C.; Howard, B. I.; Kleinjan, C.; Kolien, J.; Payet, F.; Telfer, S. G.; Kruger, P. E.; Bennett, T. D. The Thermal Stability of Metal-Organic Frameworks. *Coord. Chem. Rev.* **2020**, *419*, 213388.

(8) Umeyama, D.; Horike, S.; Inukai, M.; Itakura, T.; Kitagawa, S. Reversible Solid-to-Liquid Phase Transition of Coordination Polymer Crystals. *J. Am. Chem. Soc.* **2015**, *137*, 864–870.

(9) Bennett, T. D.; Tan, J.-C.; Yue, Y.; Baxter, E.; Ducati, C.; Terrill, N. J.; Yeung, H. H.-M.; Zhou, Z.; Chen, W.; Henke, S.; Cheetham, A. K.; Greaves, G. N. Hybrid Glasses

from Strong and Fragile Metal-Organic Framework Liquids. *Nat. Commun.* **2015**, *6*, 8079.

(10) Ma, N.; Horike, S. Metal–Organic Network-Forming Glasses. *Chem. Rev.* **2022**, *122*, 4163–4203.

(11) Xu, W.; Hanikel, N.; Lomachenko, K. A.; Atzori, C.; Lund, A.; Lyu, H.; Zhou, Z.; Angell, C. A.; Yaghi, O. M. High-Porosity Metal-Organic Framework Glasses. *Angew. Chem. Int. Ed.* **2023**, *62*, e202300003.

(12) Frentzel-Beyme, L.; Kolodzeiski, P.; Weiß, J.-B.; Schneemann, A.; Henke, S. Quantification of Gas-Accessible Microporosity in Metal-Organic Framework Glasses. *Nat. Commun.* **2022**, *13*, 7750.

(13) Frentzel-Beyme, L.; Kloß, M.; Pallach, R.; Salamon, S.; Moldenhauer, H.; Landers, J.; Wende, H.; Debus, J.; Henke, S. Porous Purple Glass – a Cobalt Imidazolate Glass with Accessible Porosity from a Meltable Cobalt Imidazolate Framework. *J. Mater. Chem. A* **2019**, *7*, 985–990.

(14) Zhou, C.; Longley, L.; Krajnc, A.; Smales, G. J.; Qiao, A.; Erucar, I.; Doherty, C. M.; Thornton, A. W.; Hill, A. J.; Ashling, C. W.; Qazvini, O. T.; Lee, S. J.; Chater, P. A.; Terrill, N. J.; Smith, A. J.; Yue, Y.; Mali, G.; Keen, D. A.; Telfer, S. G.; Bennett, T. D. Metal-Organic Framework Glasses with Permanent Accessible Porosity. *Nat. Commun.* **2018**, *9*, 5042.

(15) Bumstead, A. M.; Ríos Gómez, M. L.; Thorne, M. F.; Sapnik, A. F.; Longley, L.; Tuffnell, J. M.; Keeble, D. S.; Keen, D. A.; Bennett, T. D. Investigating the Melting Behaviour of Polymorphic Zeolitic Imidazolate Frameworks. *CrystEngComm* **2020**, *22*, 3627–3637.

(16) Gaillac, R.; Pullumbi, P.; Beyer, K. A.; Chapman, K. W.; Keen, D. A.; Bennett, T. D.; Coudert, F.-X. Liquid Metal–Organic Frameworks. *Nat. Mater.* **2017**, *16*, 1149–1154.

(17) Gaillac, R.; Pullumbi, P.; Coudert, F.-X. Melting of Zeolitic Imidazolate Frameworks with Different Topologies: Insight from First-Principles Molecular Dynamics. *J. Phys. Chem. C* **2018**, *122*, 6730–6736.

(18) Widmer, R. N.; Lampronti, G. I.; Anzellini, S.; Gaillac, R.; Farsang, S.; Zhou, C.; Belenguer, A. M.; Wilson, C. W.; Palmer, H.; Kleppe, A. K.; Wharmby, M. T.; Yu, X.; Cohen, S. M.; Telfer, S. G.; Redfern, S. A. T.; Coudert, F.-X.; MacLeod, S. G.; Bennett, T. D. Pressure Promoted Low-Temperature Melting of Metal–Organic Frameworks. *Nat. Mater.* **2019**, *18*, 370–376.

(19) Gaillac, R.; Pullumbi, P.; Bennett, T. D.; Coudert, F.-X. Structure of Metal–Organic Framework Glasses by Ab Initio Molecular Dynamics. *Chem. Mater.* **2020**, *32*, 8004–8011.

(20) Shi, Z.; Arramel, A.; Bennett, T. D.; Yue, Y.; Li, N. The Deformation of Short-Range Order Leading to Rearrangement of Topological Network Structure in Zeolitic Imidazolate Framework Glasses. *iScience* **2022**, *25*, 104351.

(21) Zomorodian, A.; Carlsson, G. Computing Persistent Homology. In *SCG '04: Proceedings of the Twentieth Annual Symposium on Computational Geometry*, **2004**, 347–356.

(22) Edelsbrunner, H.; Letscher, D.; Zomorodian, A. Topological Persistence and Simplification. In *Proceedings 41st Annual Symposium on Foundations of Computer Science*; **2000**, 454–463.

(23) Hiraoka, Y.; Nakamura, T.; Hirata, A.; Escolar, E. G.; Matsue, K.; Nishiura, Y. Hierarchical Structures of Amorphous Solids Characterized by Persistent Homology. *Proc. Natl. Acad. Sci. U.S.A.* **2016**, *113*, 7035–7040.

(24) Sørensen, S. S.; Biscio, C. A. N.; Bauchy, M.; Fajstrup, L.; Smedskjaer, M. M. Revealing Hidden Medium-Range Order in Amorphous Materials Using Topological Data Analysis. *Sci. Adv.* **2020**, *6*, eabc2320.

(25) Sørensen, S. S.; Du, T.; Biscio, C. A. N.; Fajstrup, L.; Smedskjaer, M. M. Persistent Homology: A Tool to Understand Medium-Range Order Glass Structure. *J. Non-Cryst. Solids X* **2022**, *16*, 100123.

(26) Bouëssel Du Bourg, L.; Ortiz, A. U.; Boutin, A.; Coudert, F. X. Thermal and Mechanical Stability of Zeolitic Imidazolate Frameworks Polymorphs. *APL Mater.* **2014**, *2*, 124110.

(27) Qiao, A.; Bennett, T. D.; Tao, H.; Krajnc, A.; Mali, G.; Doherty, C. M.; Thornton, A. W.; Mauro, J. C.; Greaves, G. N.; Yue, Y. A Metal-Organic Framework with Ultrahigh Glass-Forming Ability. *Sci. Adv.* **2022**, *4*, eaao6827.

(28) Qiao, A.; Sørensen, S. S.; Stepniewska, M.; Biscio, C. A. N.; Fajstrup, L.; Wang, Z.; Zhang, X.; Calvez, L.; Hung, I.; Gan, Z.; Smedskjaer, M. M.; Yue, Y. Hypersensitivity of the Glass Transition to Pressure History in a Metal–Organic Framework Glass. *Chem. Mater.* **2022**, *34*, 5030–5038.

(29) Sarkar, S.; Grønbech, T. B. E.; Mamakhel, A.; Bondesgaard, M.; Sugimoto, K.; Nishibori, E.; Iversen, B. B. X-ray Electron Density Study of the Chemical Bonding Origin of Glass Formation in Metal–Organic Frameworks. *Angew. Chem. Int. Ed.* **2022**, *61*, e202202742.

(30) Zhou, Q.; Shi, Y.; Deng, B.; Du, T.; Guo, L.; Smedskjaer, M. M.; Bauchy, M. Revealing the Medium-Range Structure of Glassy Silica Using Force-Enhanced Atomic Refinement. *J. Non-Cryst. Solids* **2021**, *573*, 121138.

(31) Biscio, C. A. N.; Møller, J. The Accumulated Persistence Function, a New Useful Functional Summary Statistic for Topological Data Analysis, With a View to Brain Artery Trees and Spatial Point Process Applications. *J. Comput. Graph. Stat.* **2019**, *28*, 671–681.

(32) Frentzel-Beyme, L.; Kloß, M.; Kolodzeiski, P.; Pallach, R.; Henke, S. Meltable Mixed-Linker Zeolitic Imidazolate Frameworks and Their Microporous Glasses: From Melting Point Engineering to Selective Hydrocarbon Sorption. *J. Am. Chem. Soc.* **2019**, *141*, 12362–12371.

(33) VandeVondele, J.; Krack, M.; Mohamed, F.; Parrinello, M.; Chassaing, T.; Hutter, J. Quickstep: Fast and Accurate Density Functional Calculations Using a Mixed Gaussian and Plane Waves Approach. *Comput. Phys. Commun.* **2005**, *167*, 103–128.

(34) Kühne, T. D.; Iannuzzi, M.; Del Ben, M.; Rybkin, V. V; Seewald, P.; Stein, F.; Laino, T.; Khaliullin, R. Z.; Schütt, O.; Schiffmann, F.; Golze, D.; Wilhelm, J.; Chulkov, S.; Bani-Hashemian, M. H.; Weber, V.; Borštnik, U.; Taillefumier, M.; Jakobovits, A. S.; Lazzaro, A.; Pabst, H.; Müller, T.; Schade, R.; Guidon, M.; Andermatt, S.; Holmberg, N.; Schenter, G. K.; Hehn, A.; Bussy, A.; Belleflamme, F.; Tabacchi, G.; Glöß, A.; Lass, M.; Bethune, I.; Mundy, C. J.; Plessl, C.; Watkins, M.; VandeVondele, J.; Krack, M.; Hutter, J. CP2K: An Electronic Structure and Molecular Dynamics Software Package - Quickstep: Efficient and Accurate Electronic Structure Calculations. *J. Chem. Phys.* **2020**, *152*, 194103.

(35) Perdew, J. P.; Burke, K.; Ernzerhof, M. Generalized Gradient Approximation Made Simple. *Phys. Rev. Lett.* **1996**, *77*, 3865–3868.

(36) Goedecker, S.; Teter, M.; Hutter, J. Separable Dual-Space Gaussian Pseudopotentials. *Phys. Rev. B* **1996**, *54*, 1703–1710.

(37) Grimme, S.; Antony, J.; Ehrlich, S.; Krieg, H. A Consistent and Accurate Ab Initio Parametrization of Density Functional Dispersion Correction (DFT-D) for the 94 Elements H-Pu. *J. Chem. Phys.* **2010**, *132*, 154104.

(38) Bennett, T. D.; Simoncic, P.; Moggach, S. A.; Gozzo, F.; Macchi, P.; Keen, D. A.; Tan, J.-C.; Cheetham, A. K. Reversible Pressure-Induced Amorphization of a Zeolitic Imidazolate Framework (ZIF-4). *Chem. Commun.* **2011**, *47*, 7983–7985.

(39) Morozov, D. Dionysus2: Persistent Homology Software. https://mrzv.org/software/dionysus2/ (accessed 2023-31-07)

(40) Morozov, D. DioDe: Persistent Homology Software. https://github.com/mrzv/diode (accessed 2023-31-07)